Energetic landscape and diffusion of He in α-Fe grain boundaries from first principles

Lei Zhang,[1,2] Chu-Chun Fu,[1,*] and Guang-Hong Lu[2,†]
[1]*CEA, DEN, Service de Recherches de Métallurgie Physique, F-91191 Gif-sur-Yvette, France*
[2]*Department of Physics, Beihang University, Beijing 100191, China*
(Received 28 January 2013; published 26 April 2013)

Combined density functional theory and empirical-potential calculations are performed to investigate the lowest-energy sites and migration mechanisms of He in various α-Fe grain boundaries (GBs). Before the defect calculations, we show that structural optimizations, including simulated annealing and atom removal, are crucial for locating the stable GB structure in a given temperature regime. Then, the He formation energies for all the substitutional and interstitial sites in two different GBs are evaluated, showing a strong He segregation tendency. At variance with the bulk Fe case, the formation energy of an interstitial He is either lower than or similar to that of a substitutional He in the GBs. Finally, both static and dynamic barriers for interstitial He diffusion in the GBs are determined. Although the diffusion details and precise paths are GB dependent, some common features are identified: (1) The He atom always remains confined to the GB region while diffusing; (2) the He diffusion is highly anisotropic along the GBs; (3) the GB diffusion of an interstitial He atom is found to be always slower than its bulk diffusion, but it can still be faster than the bulk diffusion of a substitutional He.

DOI: 10.1103/PhysRevB.87.134107 PACS number(s): 61.72.Mm, 68.35.Fx, 71.15.Mb, 71.15.Nc

I. INTRODUCTION

Grain boundary (GB) segregation of solutes strongly influences the diffusion, microstructural evolution, and mechanical behavior of polycrystalline materials. Although the atomic-scale properties, such as GB structure and solute diffusion and clustering at GBs, are of prime importance to the segregation process, they are difficult to obtain. On one side, experiments may have access to these data, but often in an indirect way.[1–4] On the other side, atomistic simulations which can provide accurate predictions of solute properties at GBs are still challenging. For instance, several first-principles studies have investigated the segregation properties of solutes at GBs in bcc metals.[5–12] However, to the best of our knowledge, only a recent density functional theory study has addressed the diffusion of H in Fe GBs.[13] The main limitations of such studies may be the very complex energetic landscapes in the presence of GBs and the high computational costs. In principle, large-scale simulations may be performed using empirical potentials (EPs), but the reliability of the results clearly depends on the ability of the EP to predict properties out of the potential fitting data, for example, the energetic landscape of solutes in a GB.

In the present work, we aim to show, by means of a combined first-principles and EP study, the importance of a proper structural optimization of even relatively simple GBs in α-Fe. We also attempt to identify the main factors which make a GB site favorable for He (a closed-shell element) segregation. Finally, we study in detail the diffusion mechanisms and barriers of a He atom in two different GBs, and compare them with the He diffusion properties in bulk Fe.

The motivation for this study comes from the necessity to understand the key atomic-scale mechanisms at the origin of He-induced intergranular embrittlement, bubble formation, and swelling of ferritic-martensitic steels, which are proposed as structural materials for future nuclear fusion devices. In the fusion environment, large amounts of helium and hydrogen (besides the vacancies and self-interstitials) are produced by nuclear transmutation due to the high-energy (14 MeV) neutron irradiation. As expected, He atoms tend to agglomerate in metals due to the extremely low solubility.[14] They can also be strongly trapped by all the structural defects containing free volume, particularly vacancies and GBs.[15–17] The properties of He in bcc-Fe GBs are of high relevance. For instance, the formation of bubbles in GBs has been suggested to contribute to high-temperature embrittlement in steels.[18–20]

He bubble nucleation at GBs has been observed experimentally in both austenitic and ferritic-martensitic steels[2,21,22] by means of transmission electron microscopy (TEM) and small-angle neutron scattering (SANS). Such He bubbles have been proposed to cause, for example, the initiation of GB cracks and premature brittle failure of stainless steels, coupled with drastic reductions in ductility under static and cyclic loads.[23] Besides the macroscopic and mechanical-property data, very little is known experimentally concerning the atomic-scale behavior of He in metal GBs. A previous study, based on TEM observations and a classical nucleation model, suggested that He diffusion along austenitic-steels GBs may be slower than interstitial He diffusion within the grains,[2] while recent thermal He desorption experiments indicated that GBs in model ferritic steels may act as easy paths for He diffusion towards surfaces.[1]

On the theoretical side, some EP simulations were undertaken to study the He segregation and diffusion at various Fe GBs.[24–26] The segregation energy of He was found to decrease linearly with increasing excess volume in the GB plane.[26] But, the He migration mechanisms and energies were found to strongly depend on temperature and on the GB types,[24,25] where no common trends were reported. Employing first-principles techniques, various studies addressed the segregation of solutes such as Ti, H, B, Co, Cr, S, and P at Fe GBs;[7–13] however, only a few works considered He, a representative example of closed-shell elements. These studies were limited to a specific Fe GB: the symmetrical tilt $\Sigma 5(310)$ GB, where the segregation energies of an isolated He and the tensile strength dependence on the He concentration in the GB[27,28] were reported.

We consider various types of symmetric tilt Fe GBs in this work—Σ5(310), Σ9(114), and Σ3(111)—in order to perform a comparative study and to draw some common conclusions, which may allow us to interpret the existing experimental evidence. In Sec. III A we first optimize the three GB structures by simulated annealing and atom removal around the GBs, similar to the method used for Si GBs.[29] Also, the vacancy formation energies around the interface are studied and rationalized in terms of the magnetovolume effect. Then in Sec. III B, we focus on the Σ5(310) and the Σ9(114) GBs, investigating the He formation energies in all possible sites and the interplay of the competing factors which contribute to the formation energies. Finally, in Sec. III C, He diffusion along the two GBs is studied.

II. METHODS OF CALCULATION

All the first-principles calculations are performed in the framework of density functional theory (DFT), as implemented in the SIESTA code.[30] The generalized gradient approximation (GGA) is used for the exchange-correlation functional in the Perdew-Burke-Ernzerhof (PBE) form. Core electrons are replaced by nonlocal norm-conserving pseudopotentials. The valence electrons are described by linear combinations of numerical pseudoatomic orbitals (LCAO). We use ten and five localized basis functions for each Fe and He atom, with largest cutoff radii of 2.95 Å and 3.22 Å, respectively.[16] The Methfessel-Paxton occupation function is used to broaden the electronic density of states with a 0.3 eV width. The valence charge density is represented using a 0.071 Å width real-space grid. The local magnetic moments are obtained from the Mulliken population analysis. The accuracy of the present approach for predicting the elementary properties of bcc Fe and He in bulk Fe is described in detail in Refs. 31 and 16, respectively. The estimated error bar for the most relevant magnitudes reported below (relative energy of two configurations and migration barriers) is around 0.05 eV.

Empirical-potential simulations are also carried out to complement the DFT calculations. They are helpful for exploring the potential-energy landscape of He and vacancies in the GBs prior to the DFT calculations, and useful for evaluating the stability of the various configurations and estimating migration barriers at finite temperatures. We employ the Ackland and Mendelev EAM potential[32] to describe Fe-Fe interactions, the Hartree-Fock-dispersion pair potential (Aziz potential) for He-He interactions,[33] and a recently published potential for Fe-He interactions.[34] This Fe-He potential, which is fitted to DFT results of the properties of an isolated He and small interstitial He and He-vacancy clusters in Fe, will be shown to satisfactorily describe the He behavior at the GBs in the present work.

Three-dimensional periodic boundary conditions are applied to all the calculations. Two equivalently but oppositely oriented GBs are included in each supercell. The initial GB structures are constructed based on the coincidence site lattice (CSL) model. The Σ5(310)/[001] GB is created by rotating two bcc grains around the [001] axis by an angle $\Theta = 36.87^\circ$. The Σ3(111)/[110] ($\Theta = 70.53^\circ$) and the Σ9(114)/[110] ($\Theta = 38.94^\circ$) GBs are constructed in a similar way. As shown in Table I, the supercell of Σ5(310) GB consists of 240 atoms.

TABLE I. Comparison of the total number of atoms in the supercell, and the formation energy of the three GBs before and after optimizations.

			GB energy (J/m^2)	
	Optimization	Atom number	DFT	EP
Σ5(310)		240	1.48	1.01
Σ9(114)	after	288	1.50	1.17
	before	288	2.09	1.64
Σ3(111)	after	284	1.51	1.26
	before	288	1.54	1.31

The x, y, and z dimensions are 8.57 Å, 9.06 Å, and 37.57 Å long, respectively, with the z direction perpendicular to the GB planes. A k-point grid of $4 \times 4 \times 1$ is used within the Monkhorst-Pack scheme. For the Σ9(114) GB, the supercell includes 288 atoms and the x, y, and z dimensions are 8.12 Å, 8.64 Å, and 49.51 Å, respectively, with a $4 \times 4 \times 1$ k-point grid. For Σ3(111) GB, the supercell contains 288 atoms, with the three dimensions equal to 8.15 Å, 14.11 Å, and 30.53 Å and a $4 \times 3 \times 2$ k-point grid. The distance between the two GBs in each supercell is larger than 15.27 Å, and the interlayer distances, the atomic volumes, and the local magnetic moments in the middle of the two GBs are comparable with the values in a perfect bcc-Fe bulk within 0.80%, 0.60%, and 1.26%, respectively. The supercells are therefore considered to be sufficiently large to avoid any direct GB-GB interaction. Here, the Voronoi polyhedra, obtained using the Voro++ code,[35] are used to characterize the atomic volumes. For the reference state of each GB calculation, supercells of the same size containing a perfect bcc bulk are used, in order to minimize the numerical error. When performing structural optimizations, using either the DFT or the EP method, all the atomic positions and the lattice vectors are allowed to change. For relaxations at 0 K, the residual forces and the stress components are smaller than 0.04 eV/Å and 0.20 GPa, respectively. Note that although the two dimensions parallel to the GB plane are expected (and confirmed) to remain at the perfect bulk values when considering clean GBs, the same fully relaxed procedure is adopted for all the cases, in order to minimize numerical errors.

To estimate interstitial He migration barriers by static calculations, we use the nudged elastic band (NEB) method[36,37] when performing EP simulations. On the other hand, the computationally more efficient drag method is used for DFT calculations, as in many of our previous studies.[16,38–41] For comparison, we have also evaluated the He migration barriers at finite temperatures with the aid of EP molecular dynamics (MD). We have performed constant-temperature MD simulations of 50 ns each between 300 K and 900 K. From these MD data, and assuming the simulation times are long enough to provide sufficient statistics, we have estimated the relative energy differences between the low-energy sites as well as the activation energies for different jump events between them.[42] To accomplish this, we have measured the total residence time at a site X (t_X), the corresponding average residence time ($\langle t_X \rangle$), the number of times that the He atom leaves a site X (n_X), and the number of times the He atom

jumps from an X to a Y site (n_{XY}), along the entire simulation time at a given temperature.

From these data, we can obtain the $X \rightarrow Y$ jump frequency by

$$\Gamma(X \rightarrow Y) = \frac{n_{XY}}{n_X \langle t_X \rangle} = \frac{n_{XY}}{t_X}. \quad (1)$$

Then, assuming the Arrhenius law, the relative residence time and the jump frequency can be respectively written as

$$\frac{t_X}{t_Y} = \exp\left[\frac{E(Y) - E(X)}{k_b T}\right] \quad (2)$$

and

$$\Gamma(X \rightarrow Y) = \Gamma_0(X \rightarrow Y) \exp\left[-\frac{E^{mig}(X \rightarrow Y)}{k_b T}\right], \quad (3)$$

where $\Gamma_0(X \rightarrow Y)$ is the pre-exponential factor, $E(Y) - E(X) \equiv \Delta E(XY)$ is the relative energy of site Y with respect to site X, and $E^{mig}(X \rightarrow Y)$ is the migration energy from X to Y. These parameters can be obtained by a linear fitting of the simulation data (t and Γ versus T).

III. RESULTS AND DISCUSSION

A. Optimization of grain-boundary structures

In the present work we consider three types of symmetrical tilt Fe GBs: $\Sigma 5(310)$, $\Sigma 9(114)$, and $\Sigma 3(111)$ GBs, showing significantly different structural properties, as described in detail in Sec. II. For instance, the tilt axis of the first GB is the [100] axis, while both the second and the third GBs have their tilt axis along the [110] direction. In addition, these two GBs [$\Sigma 9(114)$ and $\Sigma 3(111)$] with the same tilt axis present very different tilt angles, of 38.91° and 70.53° respectively. Also, it is worth mentioning that although they are rather special GBs, two of them have been observed with high-resolution transmission electron microscopy (HRTEM) and with Auger spectroscopy in some bcc metals.[43–45]

It is essential to optimize the GB structures when performing atomistic simulations, since the GB thermal stability, the preferential segregation sites and segregation energies of solutes, and the mechanism of solute diffusion in the GB may strongly depend on the GB structure. It was suggested in the case of Si GBs that the optimization can be achieved by simulated annealing at finite temperatures and atom removal around the GB plane.[29,46] After the optimization process, the GB configuration is expected to reach a lower energy state, stable against further inclusion of vacancies and self-interstitial atoms. We have therefore attempted to optimize the three Fe GB structures as follows: First, the GB systems are annealed at 600 K for 50 ps, with the EP, followed by quenching to 0 K. After this procedure, the $\Sigma 5(310)$ GB keeps the initial configuration while the $\Sigma 9(114)$ GB shows significant structural modification. Figure 1 shows the details of the configuration change before and after the thermal annealing. Two neighboring (114) layers near the GB plane merge in order to form a new GB plane. Simultaneously, one of the grains shifts by 13.7% of the entire supercell length in the $[\bar{2}2\bar{1}]$ direction to match the other grain, recovering the mirror symmetry. We note that this process is actually equivalent to adding two self-interstitial atoms in the GB plane. The $\Sigma 9(114)$ GB energy

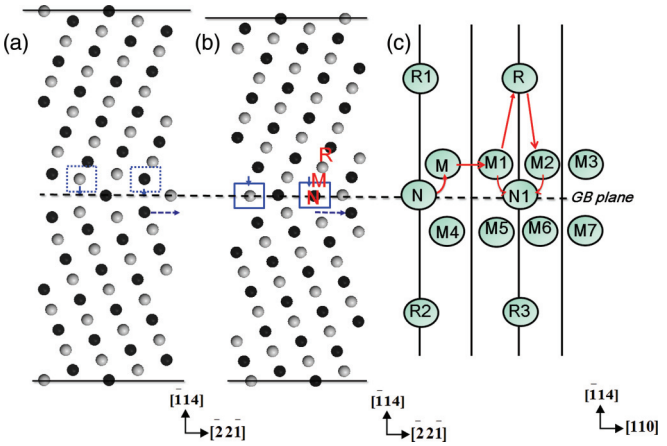

FIG. 1. (Color online) Atomic configurations of $\Sigma 9(114)$ GB (a) before and (b) after structural optimization. The black and gray spheres represent atoms in different (110) layers. The arrows indicate atom displacements during the optimization. (c) is a partial side view showing the diffusion paths of an interstitial He. The letters M, N, and R indicate the low-energy sites of an interstitial He; all the Mi, Ni, and Ri are equivalent to M, N, and R, respectively. The red arrows in (c) indicate the two possible diffusion paths: $N \rightarrow M \rightarrow M1 \rightarrow N1$, and $N \rightarrow M \rightarrow M1 \rightarrow R \rightarrow M2 \rightarrow N1$.

decreases from 1.64 J/m^2 to 1.17 J/m^2 according to the EP. This optimized GB configuration is also verified and confirmed by DFT calculations. The corresponding GB energy reduction is 0.59 J/m^2. The GB formation energy $E^f(GB)$ is calculated by

$$E^f(GB) = \frac{E(GB) - E(bulk)}{2S}, \quad (4)$$

where $E(GB)$ is the total energy of supercell with the GBs, $E(bulk)$ is the total energy of the bulk crystal with the same number of atoms, and S is the area of the GB plane within the supercell.

On the other side, the $\Sigma 3(111)$ GB is revealed to be unstable during the annealing, and the system decays to a perfect bcc state. In order to understand this thermal instability, we have calculated the vacancy formation energies close to the GB [$E^f(vac)$], defined as

$$E^f(vac) = E_{GB}(vac) - E_{GB}(clean) + E_{bulk}(\mathrm{Fe}), \quad (5)$$

where $E_{GB}(vac)$ is the energy of the relaxed GB with a vacancy, $E_{GB}(clean)$ is the energy of the clean GB, and $E_{bulk}(\mathrm{Fe})$ is the energy of a Fe atom in a perfect bcc bulk.

When a monovacancy is introduced around the $\Sigma 3(111)$ GB plane ($L0$), negative vacancy formation energies appear at the first and second nearest neighboring layers of the interface ($L1$ and $L2$) based on DFT data (Fig. 2). The corresponding EP values are also shown for comparison. They are qualitatively similar to the DFT results. The negative vacancy formation energies indicate that creating a vacancy in either the $L1$ or the $L2$ layer decreases the system energy so that the initial $\Sigma 3(111)$ GB configuration is not energetically stable. To look for a more stable configuration, we have calculated the vacancy formation energies considering various possible combinations of vacancies in $L1$ and $L2$ layers, as shown in Fig. 2. As a result, we have found 9 combinations of two-vacancy configurations

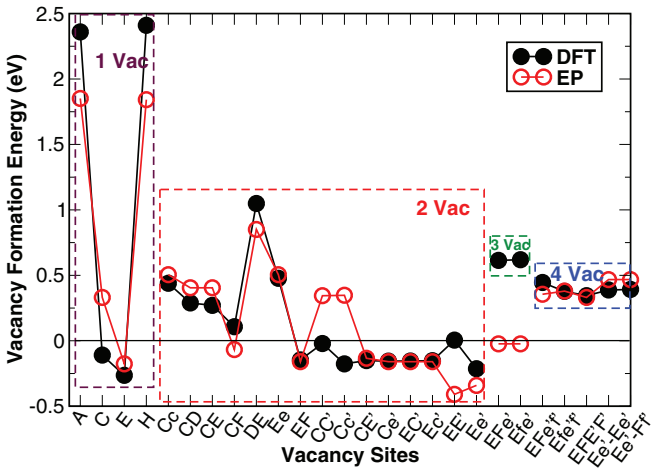

FIG. 2. (Color online) Formation energies $E^f(vac)$ of 1, 2, 3, and 4 vacancies in the $\Sigma3(111)$ GB. The vacancy sites correspond to the letters marked in Fig. 3. For 4 vacancies, the Ee'-Ee' and Ee'-Ff' configurations mean removing two atoms (Ee') from one grain and removing two other atoms (either Ee' or Ff') from the other grain.

which result in negative formation energies. Among them, the Ee' configuration shows the lowest value. We note that when two atoms at the E and e' sites are removed, the $L1$ and the $L2$ atoms merge, forming a single layer, which is the new GB plane (new $L0$ layer), as shown in Fig. 3. Starting from this new Ee' configuration, if we continue removing more atoms, the obtained vacancy formation energies are all positive [Fig. 4(c)]. We therefore propose this Ee' configuration to be the lowest-energy ordered structure for the $\Sigma3(111)$ GB using the present approach [Fig. 3(b)], at least close to 0 K. At variance with the initial structure and due to its reduced symmetry, various atoms at either the interface or the sub-interface layers are nonequivalent. The obtained DFT GB formation energy is 1.51 J/m^2, that is, 0.03 J/m^2 lower than that of the nonoptimized structure (Table I). It is worth mentioning that ordered structures were also found to be stable at finite temperatures by atomistic simulations for special Si GBs, in agreement with experimental evidence.[29]

In order to compare the thermal stability of the new and the original $\Sigma3(111)$ GB structures, various EP annealings of 1 ns each were carried out between 100 K and 500 K. We find that the new configuration is stable up to 400 K while the original structure is already unstable after a few picoseconds at 100 K. Above these limit temperatures, both the initial and the new GBs decay to a perfect bcc structure. Obviously, these simulations do not allow conclusions about the absolute thermal stability of the new structure at any finite temperature, but they do confirm the relative stability of the two configurations. In summary, even though the initial structure is only 0.03 J/m^2 above the new GB structure, two strong reasons support the instability of the former: the negative formation energy of a single vacancy (−0.26 eV) or a divacancy (−0.21 eV), as well as its poor thermal stability. It is important to point out that a large number of previous DFT and EP works have addressed properties of the Fe $\Sigma3(111)$ GB, including solutes segregation. They have all considered the original unstable structure,[9,11,12,26,47–52] constructed based on the CSL model. These previous results and some of their conclusions may be worth revising based on the present finding.

We have also calculated the vacancy formation energies close to the $\Sigma5(310)$ and $\Sigma9(114)$ GBs, using the post-thermal annealing structures. All the values are positive as shown in Figs. 4(a) and 4(b), indicating that the present structures of $\Sigma5(310)$ and $\Sigma9(114)$ GBs are stable against further inclusion of vacancies. From Figs. 5(a) and 1(b), it is clear that both $\Sigma5(310)$ and $\Sigma9(114)$ GBs show mirror symmetry. The resulting DFT GB formation energies are 1.48 J/m^2 and 1.50 J/m^2, respectively. The properties of the three GBs, before and after structural optimization, are summarized in Table I.

We next analyze in more detail the vacancy formation energies in the three GBs, based on their respective optimized structures. As shown in Fig. 4, the vacancy formation energies range from 0.41 eV to 2.32 eV close to the GBs. As expected,

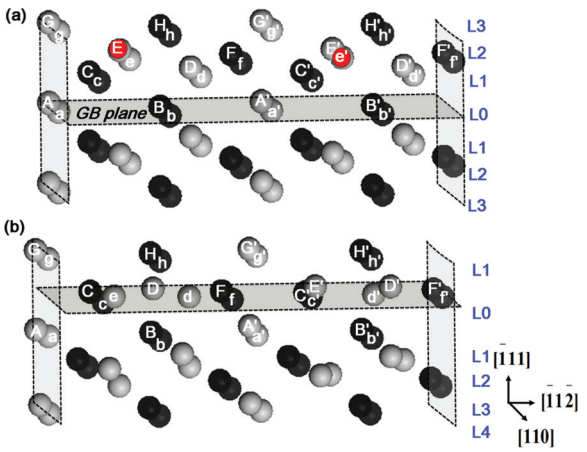

FIG. 3. (Color online) $\Sigma3(111)$ GB configurations (a) before and (b) after structural optimization. The black and gray spheres indicate the atoms in different (110) layers. The GB planes are indicated by the horizontal planes. In the optimized structure (b), the two red atoms E and e' in the $L2$ layer are removed.

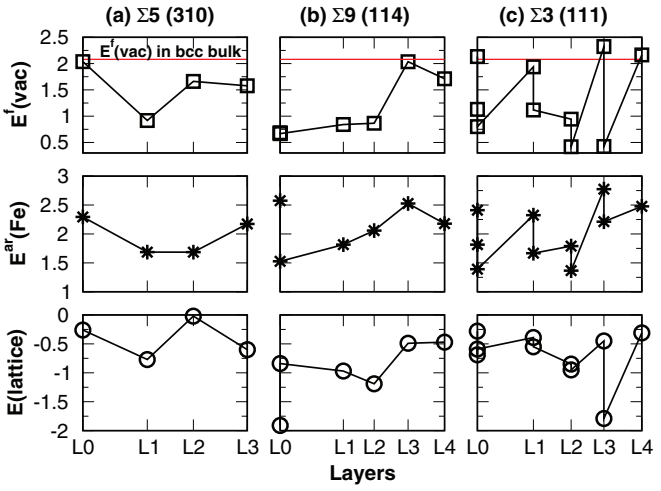

FIG. 4. (Color online) DFT vacancy formation energies $E^f(vac)$ (eV), atom removal energies E^{ar}(Fe) (eV), and lattice relaxation energies $E(lattice)$ (eV) at the neighboring atomic layers of (a) $\Sigma5(310)$, (b) $\Sigma9(114)$, and (c) $\Sigma3(111)$ GBs.

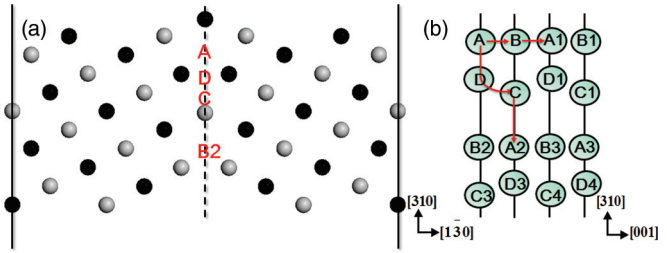

FIG. 5. (Color online) (a) Atomic configuration and (b) a top view of the GB plane showing the diffusion path of an interstitial He in Σ5(310) GB. The black and gray spheres indicate the atoms in different (001) layers. The letters A, B, C, and D represent the low-energy sites of an interstitial He; all the Ai, Bi, Ci, and Di are equivalent to A, B, C, and D, respectively. The red arrows in (b) indicate the two possible diffusion paths: $A \rightarrow B \rightarrow A1$, and $A \rightarrow D \rightarrow C \rightarrow A2$.

the values are much lower than the formation energy of 2.08 eV in the bcc bulk. To verify the accuracy of these values, we have checked that the formation energy of a vacancy in the middle of a grain converges to the bcc bulk value with a precision better than 0.58%, for all the three GBs. Close to the Σ9(114) GB, the lowest-energy site of a vacancy lies at the GB plane ($L0$), whereas the situation is different in the other two GBs. The lowest-energy vacancy sites are found at the $L1$ and the $L2$ planes of the Σ5(310) and the Σ3(111) GBs, respectively. In order to better understand the origin of the relative vacancy stability at the various layers close to a GB, we split the vacancy formation energy $E^f(vac)$ into an atom-removal (ar) energy [E^{ar}(Fe)] and a lattice relaxation energy [$E(lattice)$]:

$$E^{ar}(\mathrm{Fe}) = E_{GB}^{non,relax}(vac) - E_{GB}(clean) + E_{bulk}(\mathrm{Fe}) \quad (6)$$

and

$$E(lattice) = E_{GB}(vac) - E_{GB}^{non,relax}(vac), \quad (7)$$

where $E_{GB}^{non,relax}(vac)$ is the energy of the GB with a vacancy before any structural relaxation. Thus, E^{ar}(Fe) is the unrelaxed vacancy formation energy, while $E(lattice)$ reflects the amount by which the atoms relax. From Fig. 4, we see that the two terms represent competing factors where generating a vacancy increases energy and lattice relaxation reduces energy. Note that although the lattice relaxation term is overall small, both contributions are of a similar order of magnitude. They therefore jointly dictate the vacancy formation energy. A typical example is the two nonequivalent vacancy sites in the $L0$ layer of Σ9(114) GB. One of them has a higher atom removal energy and a lower lattice relaxation energy while the situation is the opposite for the other site. However, the competitions result in a very similar vacancy formation energies, the difference being only 0.02 eV.

We are particularly interested in understanding the atom-removal energy variation at different layers close to a GB. First, we checked that there is no clear relationship between this term and the Voronoi volume of the atoms. However, the local magnetic moment variation μ^{var}, reflecting the electronic-magnetic redistribution, may be helpful to analyze the origin of the E^{ar}(Fe) variation. Taking as references the local magnetic moments of the clean-GB system, μ^{var} is

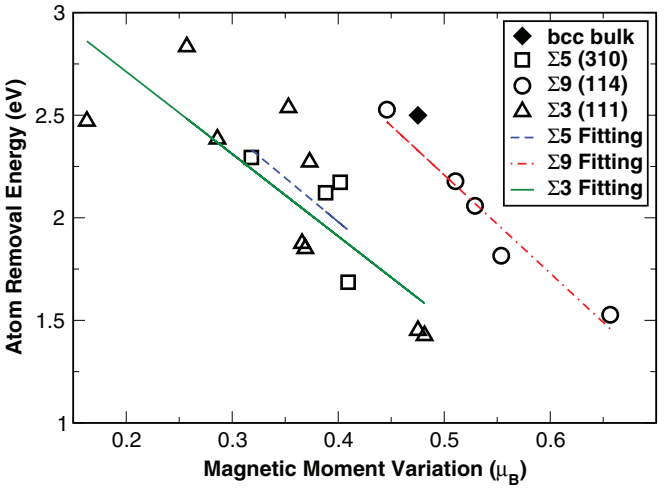

FIG. 6. (Color online) Atom removal energy E^{ar}(Fe) versus local magnetic moment variation μ^{var} in Σ5(310), Σ9(114), and Σ3(111) GBs.

evaluated by

$$\mu^{var} = \sqrt{\Sigma[\mu_i(vac) - \mu_i(clean)]^2}, \quad (8)$$

where $\mu_i(vac)$ is the local magnetic moment of the ith Fe atom in the system containing the vacancy and $\mu_i(clean)$ is the local moment of the corresponding atom in the corresponding clean-GB system. Note that only those atoms with a local moment variation larger than the calculation precision limit (0.05 μ_B) are taken into account. For example, in Σ5(310) GB, 8 atoms surrounding the vacancies at the $L0$, the $L2$, or the $L3$ layers and 7 atoms surrounding the vacancy at the $L1$ layer are considered. The variations are mainly due to the increase of the local magnetic moments of the atoms around the vacancies, but a few atoms also show a significant decrease of the local moments. From Fig. 6, we note a roughly linear relationship between μ^{var} and E^{ar}(Fe), where E^{ar}(Fe) generally decreases with increasing μ^{var}. This phenomenon may be interpreted in terms of the well-known magnetovolume effect.[53–55] The magnetic redistribution, taken as an additional degree of freedom in magnetic materials such as Fe, may contribute to lowering the energy of the system in the presence of structural defects. We see from Fig. 6 that the Σ9(114) GB shows a linear behavior more clearly than the Σ5(310) and Σ3(111) GBs. The data of a vacancy in a perfect bcc bulk is also given as a reference. In order to compare with the DFT data, we have also calculated the relaxed and unrelaxed vacancy formation energies using the EAM potential. We noted that the relaxed values are in very good agreement with the DFT values, but the unrelaxed vacancy formation energies, particularly for the sites around the GBs, are generally larger. A possible reason is indeed the lack of the extra magnetic freedom in the EAM potential.

B. Energetic landscape of He in grain boundaries

In the present work, we focus on the Σ5(310) and Σ9(114) GBs to explore the effect of He. Geometrically, there are 26 different interstitial sites in the core of the Σ5(310) GB, that is, from the GB plane ($L0$) to the $L3$ layer. Similarly, there

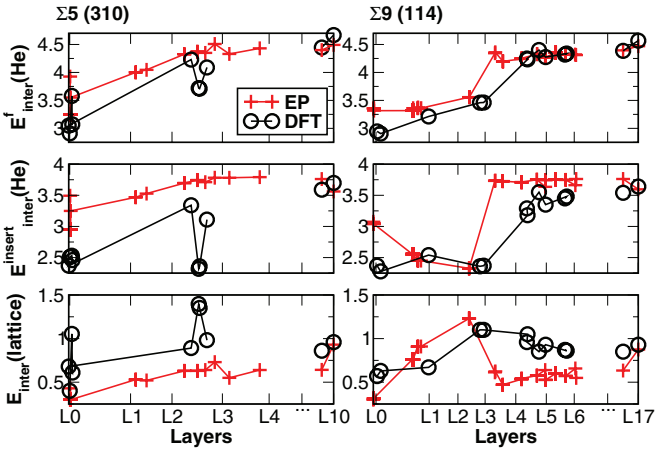

FIG. 7. (Color online) He formation energies E^{f}_{inter}(He) (eV), He insertion energies E^{insert}_{inter}(He) (eV), and lattice relaxation energies $E_{inter}(lattice)$ (eV), for an interstitial He at different layers of Σ5(310) and Σ9(114) GBs perpendicular to the GB plane.

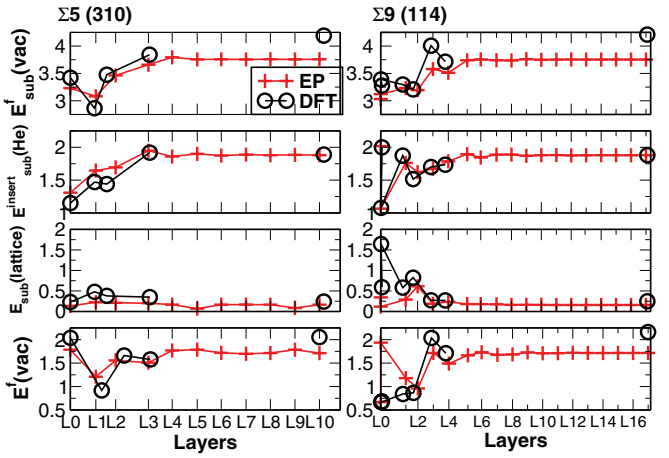

FIG. 8. (Color online) He formation energies E^{f}_{sub}(He) (eV), He insertion energies E^{insert}_{sub}(He) (eV), lattice relaxation energies $E_{sub}(lattice)$ (eV), and vacancy formation energies $E^{f}(vac)$ (eV) for a substitutional He at different layers of Σ5(310) and Σ9(114) GBs perpendicular to the GB plane.

are 59 interstitial sites from $L0$ to $L6$ layer in the Σ9(114) GB. All of these possible GB configurations containing one He atom are first relaxed with EP. After relaxation, only 11 nonequivalent interstitial cases remain for both Σ5(310) and Σ9(114) GBs, as shown in Fig. 7. These nonequivalent sites are then considered with the DFT method. For Σ5(310) GB, 7 nonequivalent configurations are obtained after the DFT optimization, where 5 of them coincide with the configurations found with EP. The lowest formation energy is 2.91 eV, found when He is at the "A" site in the $L0$ layer, as indicated in Fig. 5. For the Σ9(114) GB, we also obtain 7 nonequivalent configurations after DFT relaxation, and 6 of them match the configurations found during the EP search. The interstitial site near the GB plane which shows the lowest formation energy, of 2.91 eV, is the "N" site in $L0$ layer, as shown in Fig. 1. Note that the same minimum value for formation energy in the Σ9(114) and Σ5(310) GBs is a pure coincidence.

For the substitutional He case, the EP method is also employed for a preliminary study of the formation energy with increasing distance from the GB plane, as shown in Fig. 8. The results show that beyond the $L3$ layer in the Σ5(310) GB and the $L4$ layer in the Σ9(114) GB, the formation energies of a substitutional He converge approximately to the bulk value. We therefore only consider the substitutional He sites up to the $L3$ and the $L4$ layers in the Σ5(310) and the Σ9(114) GBs, respectively, in DFT optimizations. The lowest formation energy obtained for a substitutional He is 2.86 eV in the $L1$ layer of the Σ5(310) GB and 3.21 eV in the $L2$ layer of the Σ9(114) GB.

Figures 7 and 8 also show a satisfactory agreement of the He formation energy between DFT and EP methods, indicating that the present EP is able to give a reasonable description of the He energetics in the GB environments. Based on these figures, we first note a significant decrease of He formation energy around the GB plane compared to that in the volume. It is also important to point out that the formation energy of an interstitial He may be either lower than or close to that of a substitutional He in these GBs. This is different from the case of bcc bulk, where He clearly prefers to stay at a substitutional site, with a formation energy 0.19 eV below the interstitial-He formation energy. The lowest-energy interstitial sites for He are all located at the GB plane for both Σ5(310) and Σ9(114) GBs. On the other hand, the preferential substitutional sites are found at the sub-interface layers, that is, at $L1$ and $L2$, respectively.

To better understand the relative energetic stability between the various He sites, the formation energy of He may be decomposed into a He-related part and a lattice-related part, similar to the vacancy formation energy in the previous section. For the interstitial case, the He formation energy E^{f}_{inter}(He) consists of a He insertion term E^{insert}_{inter}(He) and a lattice relaxation term $E_{inter}(lattice)$:

$$E^{f}_{inter}(\mathrm{He}) = E^{insert}_{inter}(\mathrm{He}) + E_{inter}(lattice), \tag{9}$$

where

$$E^{insert}_{inter}(\mathrm{He}) = E_{GB\text{-}inter}(\mathrm{He}) - E_{GB\text{-}inter}(non,\mathrm{He}) - E(\mathrm{He}) \tag{10}$$

and

$$E_{inter}(lattice) = E_{GB\text{-}inter}(non,\mathrm{He}) - E_{GB}(clean), \tag{11}$$

where $E_{GB\text{-}inter}$(He) is the energy of the relaxed GB with an interstitial He atom and $E_{GB\text{-}inter}(non,\mathrm{He})$ is the energy of the identical system without the He atom. E(He) is the energy of an isolated He atom, and $E_{GB}(clean)$ is the energy of the relaxed clean GB. For the substitutional case, the He formation energy E^{f}_{sub}(He) consists of the He insertion term E^{insert}_{sub}(He), the lattice relaxation term $E_{sub}(lattice)$, and the vacancy formation energy $E^{f}(vac)$:

$$E^{f}_{sub}(\mathrm{He}) = E^{insert}_{sub}(\mathrm{He}) + E_{sub}(lattice) + E^{f}(vac). \tag{12}$$

The definition of E^{insert}_{sub}(He) is similar to E^{insert}_{inter}(He), and $E_{sub}(lattice)$ is calculated by

$$E_{sub}(lattice) = E_{GB\text{-}sub}(non,\mathrm{He}) - E_{GB}(vac), \tag{13}$$

where $E_{GB}(vac)$ is the energy of the relaxed GB with a vacancy.

Figures 7 and 8 present the contribution of each part to the He formation energy at various layers from the GB plane. In the interstitial case, the contribution of the He insertion term is overall dominant, whereas that of the lattice relaxation term is smaller but not negligible. Taking as an example the interstitial He located between $L2$ and $L3$ of the $\Sigma5(310)$ GB in Fig. 7, the He insertion term has the lowest value among all the considered sites, but the lattice relaxation energy shows the highest value. As a result, this site is clearly not the lowest-energy site for He.

For the substitutional He case, we note that both vacancy-formation and He insertion terms make similar contributions. The lattice relaxation energy is generally small, consistent with the fact that introducing a He atom into a vacancy in bulk Fe does essentially not cause further lattice distortion. The situation is different only for the sites close to the $\Sigma9(114)$ GB plane, which show a large deviation of Fe Voronoi volumes with respect to that in the bulk, from -5.2% to 22.6%. Large atomic displacements may therefore occur upon putting He into a vacancy. For comparison, the Voronoi-volume change around the $\Sigma5(310)$ GB plane is significantly smaller, ranging from -0.8% to 14.7%.

In addition, we try to gain more insight into the He insertion term. When performing an EP calculation, the total energy is the sum of the energies of each atom; thus the energy of a He atom near the GBs can be easily obtained. Figure 9 shows a perfect linear relationship between the He insertion term and the He-atom energy near the GBs. On the other hand, although the energy of a He atom cannot be directly obtained from DFT calculations, the dependence of the He insertion term on the He property may be obtained indirectly. In particular, it is well known that the presence of free volume may lower the metal-system energy with He.[16,56] We therefore attempt to correlate the Voronoi volume of a He atom with its corresponding insertion energy. As shown in Fig. 10, a linear relationship is found between them.

Based on this result, the formation energy of an interstitial He $E^f_{inter}(\mathrm{He})$ can be written as

$$E^f_{inter}(\mathrm{He}) = \alpha_{inter} V^{Voro}_{inter}(\mathrm{He}) + E_{inter}(lattice) + c_{inter}. \quad (14)$$

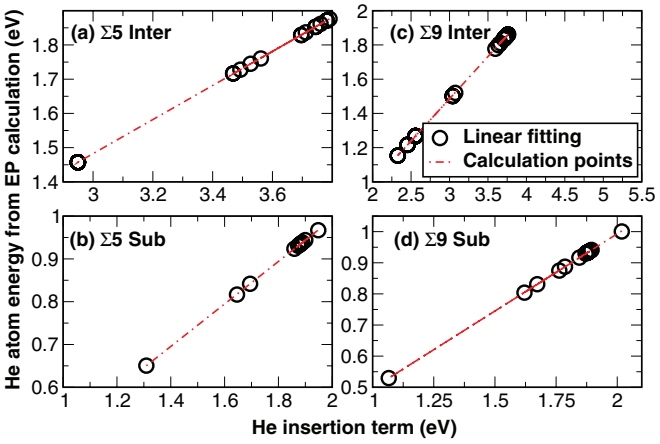

FIG. 9. (Color online) He atom energy from EP method versus He insertion energy in $\Sigma5(310)$ and $\Sigma9(114)$ GBs. Data are shown for all the substitutional sites and the interstitial sites up to the sixth atomic layer from the GB.

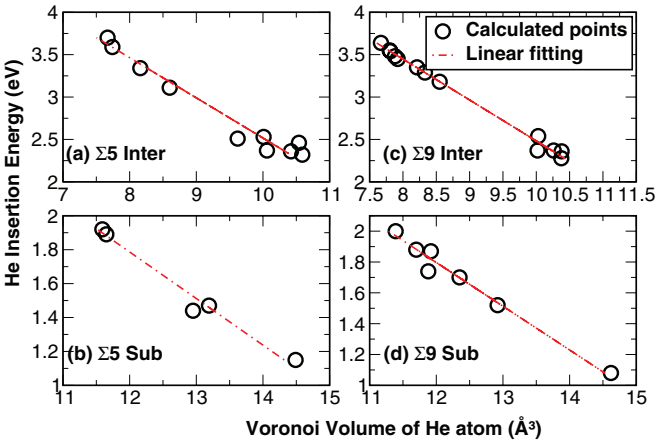

FIG. 10. (Color online) He insertion energy versus the Voronoi volume of He atom from DFT calculations in $\Sigma5(310)$ and $\Sigma9(114)$ GBs.

Similarly, the formation energy of a substitutional He, in a preexisting vacancy, can be expressed as

$$E^f_{sub}(\mathrm{He}) - E^f(vac) = \alpha_{sub} V^{Voro}_{sub}(\mathrm{He}) + E_{sub}(lattice) + c_{sub}, \quad (15)$$

where α_{inter}, α_{sub}, c_{inter}, and c_{sub} can be obtained by a planar fitting, as shown in Fig. 11. Negative values of α_{inter} and α_{sub} were obtained, confirming the decrease of He formation energy with increasing He volume. But again, the quantitative value of the formation energies are determined by the interplay of two competing contributions: the volume occupied by the He atom and the distortion of the Fe lattice caused by the presence of He.

We next seek to compare the lowest energy configurations of He at the two GBs. For the interstitial case, the formation energies are 2.91 eV in both $\Sigma5(310)$ and $\Sigma9(114)$ GBs, while

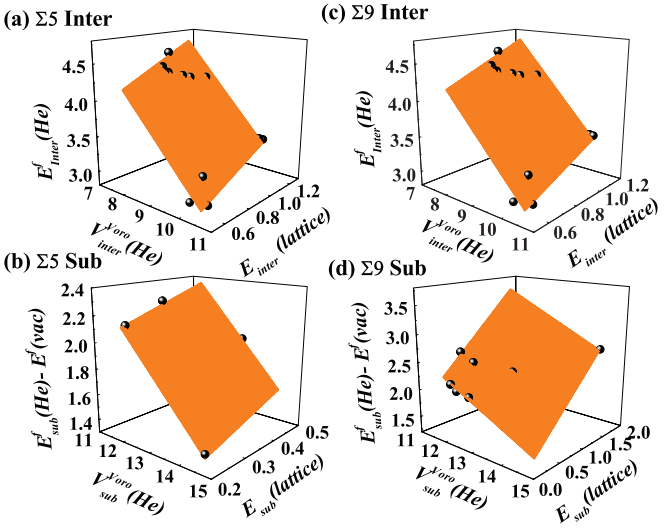

FIG. 11. (Color online) He formation energy $E^f(\mathrm{He})$ (eV) as a function of the He Voronoi volume $V^{Voro}(\mathrm{He})$ (Å^3) and the lattice relaxation energy $E(lattice)$ (eV) for the interstitial and substitutional sites in $\Sigma5(310)$ and $\Sigma9(114)$ GBs. The black spheres represent the DFT points, and the orange planes are obtained by fitting.

the formation energies of a substitutional are 2.83 eV and 3.21 eV, respectively. In order to compare with the EP data from Kurtz *et al.*,[26] we attempt to correlate the formation energy and the GB excess volume, being this one of the characteristic properties of a GB. The GB excess volume per area of GB plane, V_{GB}/S, is defined as in the study from Kurtz *et al.*, as the sum of the Voronoi volume variation of all the atoms in one grain over the area of the GB plane. The Voronoi volume of an Fe atom in a bcc bulk is taken as a reference. The values of V_{GB}/A in the $\Sigma5(310)$ and the $\Sigma9(114)$ GBs are 0.42 Å and 0.33 Å, respectively. In the present case, there is not an obvious correlation found between the GB excess volume and the He formation energy, at variance with the conclusion reported in Ref. 26.

C. Diffusion of He in grain boundaries

The diffusion properties of an interstitial He atom in $\Sigma5(310)$ and $\Sigma9(114)$ GBs are studied in detail. Finite-temperature MD simulations with an EP are first carried out to explore all the possible diffusion paths. Then, static EP and DFT calculations are performed to compute the most relevant migration barriers.

Figures 12 and 13 show the DFT migration barriers between the neighboring local minima, represented in Figs. 5 and 1, respectively. The corresponding barriers obtained by static EP calculations are also shown for comparison. We first focus on the DFT results. There are three local energy minima in both $\Sigma5(310)$ and $\Sigma9(114)$ GBs, which are the positions A, C, D [Figs. 5(a) and 5(b)], and N, M, R [Figs. 1(b) and 1(c)], respectively. Among them, A in $\Sigma5(310)$ GB and N in $\Sigma9(114)$ GB are the lowest-energy interstitial sites. Values for relative energy differences and migration barriers between these local minima are summarized in Tables II and III. Please note that, based on 0 K structural optimizations described in Sec. III B, the B site in the $\Sigma5(310)$ GB is also found as a local minimum for an interstitial He atom. However, it is proved to actually be a saddle point when performing barrier calculations, as shown in Fig. 12.

According to our results, the He migration in $\Sigma5(310)$ consists in successive jumps, all parallel to the GB plane [Figs. 5(b) and 12]. In the $\Sigma9(114)$ GB, although the He atom may perform jumps away from the GB plane, its long-range migration is still confined to be parallel to the interface, within a distance of ∼2.5 Å [Fig. 1(c)]. In order to perform a more detailed analysis of the He migration paths, we define that in

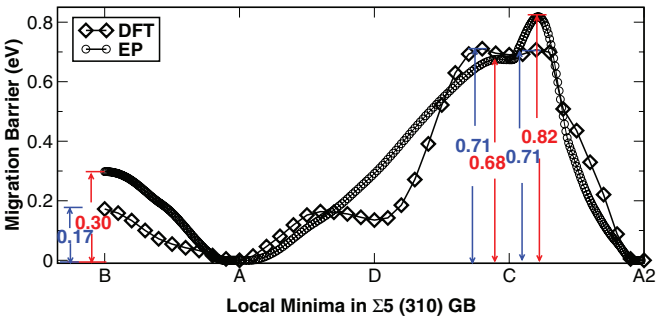

FIG. 12. (Color online) Static migration barriers of an interstitial He between the local minima in $\Sigma5(310)$ GB at 0 K.

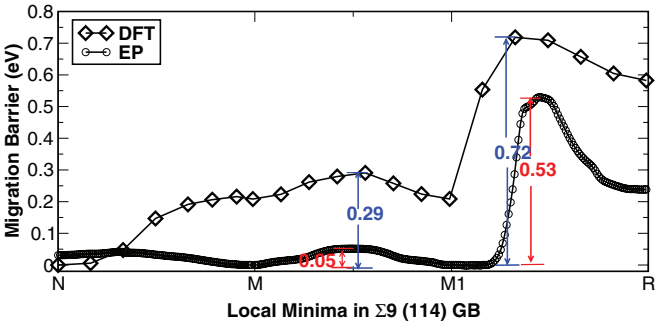

FIG. 13. (Color online) Static migration barriers of an interstitial He between the local minima in $\Sigma9(114)$ GB at 0 K.

the $\Sigma5(310)$ GB, [001] is the x direction and [310] is the y direction. Similarly, in the $\Sigma9(114)$ GB, [110] and $[\bar{1}14]$ are taken as respectively the x and the z directions.

Concerning the migration of an interstitial He in the $\Sigma5(310)$ GB, the He jumps can be sorted into three types according to their jump directions: x, y, and xy. For instance, $A \leftrightarrow B$ is an x jump, $D \leftrightarrow C$ is an xy jump, and $A \leftrightarrow D$ and $C \leftrightarrow A2$ are y jumps [Fig. 5(b)]. The He atom has two different diffusion paths along the $\Sigma5(310)$ GB: (1) always performing x jumps to diffuse one-dimensionally (1D) along a given [001] direction through an $A \rightarrow B \rightarrow A1$ path; (2) taking both y and xy jumps to diffuse parallel the GB plane through an $A \rightarrow D \rightarrow C \rightarrow A2$ path [Fig. 5(b)]. Of course, any combination of paths (1) and (2) is also allowed. When looking at the corresponding migration barriers, we find a much lower barrier for the 1D diffusion (0.17 eV) than for the zigzag two-dimensional (2D) diffusion (0.71 eV). Therefore, an interstitial He in a $\Sigma5(310)$ GB is expected to primarily undergo 1D diffusion combined with occasional reorientations. It is also interesting to mention that a recent DFT study[13] predicted the same 1D path for a H atom diffusion in the $\Sigma5(310)$ GB.

For the $\Sigma9(114)$ GB, the jumps of He atoms can be sorted into x and xz types. For example, $M \leftrightarrow M1$ is an x jump, and $N \leftrightarrow M$ and $M1 \leftrightarrow R$ are xz jumps. A He atom has also two different diffusion paths along the $\Sigma9(114)$ GB: either taking only close-neighbor jumps through a $N \rightarrow M \rightarrow M1 \rightarrow N1$ path or performing long jumps through a $N \rightarrow M \rightarrow M1 \rightarrow R \rightarrow M2 \rightarrow N1$ path. In the former case, a low barrier of 0.29 eV is required while the barrier for the latter path is

TABLE II. Relative energy differences between the initial and the final states ΔE (eV), migration barriers E^{mig} (eV), and pre-exponential factors of the jump frequencies Γ_0 (1/s) between the local minima of an interstitial He in $\Sigma5(310)$ GB at 0 K (static) and finite temperatures (dynamic).

	DFT		EP (static)		EP (dynamic)		
	ΔE	E^{mig}	ΔE	E^{mig}	ΔE	E^{mig}	Γ_0
$A \rightarrow A1$	0.00	0.17	0.00	0.30	0.00	0.26	6.18×10^{11}
$A \rightarrow D$	0.14	0.16	0.29				
$D \rightarrow C$	0.56	0.58	0.38				
$A \rightarrow C$	0.69	0.71	0.67	0.82	0.67	0.62	1.93×10^{12}
$A2 \rightarrow C$	0.69	0.71	0.67	0.68	0.67	0.68	3.62×10^{12}

TABLE III. Relative energy differences between the initial and the final states ΔE (eV), migration barriers E^{mig} (eV), and pre-exponential factors of the jump frequencies Γ_0 (1/s) between the local minima of an interstitial He in $\Sigma 9(114)$ GB at 0 K (static) and finite temperature (dynamic).

	DFT		EP (static)		EP (dynamic)		
	ΔE	E^{mig}	ΔE	E^{mig}	ΔE	E^{mig}	Γ_0
$N \rightarrow M$	0.21	0.22	0.03	0.01	0.05		
$M \rightarrow N$	0.21	0.01	0.03	0.04	0.05	0.04	1.45×10^{12}
$M \rightarrow M1$	0.00	0.08	0.00	0.05	0.00	0.08	2.72×10^{11}
$M1 \rightarrow R$	0.37	0.53	0.24	0.53	0.22	0.14	3.36×10^{11}

significantly higher (0.72 eV), as shown in Fig. 13. It is important to mention that both the paths imply an 1D diffusion, along a given x ([110]) direction. Also, as the R site is located between the $L2$ and the $L3$ layers (Fig. 1), along the latter path, the He atom can still be confined within three layers perpendicular to the GB plane despite the long jumps.

In order to understand He diffusion in the GBs, it is indispensable to compare the probability of He migration parallel to the GB plane, as described above, to that of He migration towards the volume (the He-GB dissociation). The He_{inter} dissociation barrier from the GB can be reasonably approximated by the sum of the He_{inter} migration energy in bulk Fe (0.06 eV)[16] and the largest He_{inter}-GB binding energy, that is, the difference between the He_{inter} formation energies in the bulk and at the preferential site in the GB. The obtained values for both the $\Sigma 5(310)$ and $\Sigma 9(114)$ GBs are 1.54 eV, much higher than the highest migration barrier found (0.72 eV). Therefore, the He mobility is expected to be mainly parallel to the GB plane without going back to the volume.

It is of interest to notice that an interstitial He atom always sees a larger barrier to diffuse along both of the GBs than in the bulk (0.06 eV), in agreement with the predicted H diffusion data in bcc Fe.[13] This conclusion was also reached by a previous experimental-modeling study on He in austenitic steels.[2] However, this does not necessarily imply that a single He diffusion along Fe GBs is slower than in the bcc bulk. Most of the He atoms are substitutional in the Fe bulk,[16] while more He tends to occupy interstitial sites in the GBs (Sec. III B). Diffusion of a single He atom is therefore expected to be dictated by the substitutional (interstitial) He migration in the bulk (GBs). In the bcc crystal, a substitutional He atom may diffuse via various mechanisms, in particular, the vacancy mechanism and the dissociative mechanism, as explained in detail in Ref. 16. Please note that the diffusion mechanism of a substitutional He appears to be quite different from a standard substitutional solute (Cu, Cr, Si, etc.), due to the strong potency of He to induce vacancy clustering, and the preference of He to stay at the center of a divacancy or any vacancy cluster.[16] As a result, the presence of He and abundant vacancies will rather induce the formation of bubbles/cavities, as observed experimentally. The mobility of He, trapped in the bubbles, tends to significantly decrease. Consistently, previous theoretical and experimental studies[57,58] suggested that the dominant mechanism for substitutional He diffusion in bulk Fe, in the presence of abundant vacancies, was by dissociation. By this mechanism, a substitutional He dissociates from its vacancy to migrate through interstitial sites until it is trapped by another vacancy. The estimated energy barrier lies between 0.24 eV and 2.36 eV.[16] These values correspond to the limiting regimes with solely thermal vacancies or an oversaturation of vacancies, respectively. Taking into account that the insertion of He in Fe crystal, by either implantation or irradiation, always introduces additional free vacancies, the diffusion barrier of a substitutional He atom in the bulk is generally higher than the lower limit (0.24 eV), and higher than that of fast interstitial He diffusion along a GB [0.17 eV or 0.29 eV for $\Sigma 5(310)$ or $\Sigma 9(114)$, respectively]. This result suggests that GBs may provide easy channels for single He diffusion in Fe. Interestingly, it is consistent with data from recent thermal He desorption experiments, using samples with various grain sizes.[1] However, please note that this modeling-experimental comparison is still preliminary, since the diffusion flux of He in the bulk and along the GBs can be modified due to He clustering. The diffusion of He in the presence of a large variety of He and He-vacancy clusters is a complex issue, not accessible by the present methods. It is therefore out of the scope of this study.

From the static barriers calculations using the EPs, the interstitial He diffusion mechanisms are overall similar to those from DFT (Figs. 12 and 13). For instance, in the $\Sigma 5(310)$ GB, the barrier for 1D diffusion (0.30 eV) is clearly lower than that for 2D diffusion (0.82 eV). Additionally, in the $\Sigma 9(114)$ GB, the barrier for the $M \leftrightarrow N \leftrightarrow M1$ path is 0.05 eV, which is much lower than that for the long jump diffusion path ($M \leftrightarrow M1 \leftrightarrow R \leftrightarrow M2$), i.e., 0.53 eV. However, some minor differences exist between the EP and the DFT results. For example, the D site in the $\Sigma 5(310)$ GB is not a local minimum for the He interstitial when using the EPs. Also, in the $\Sigma 9(114)$ GB, the relative stability of the N and the M sites is reversed with respect to the DFT results. For a further comparison between DFT and EP data, the relative energy differences, the migration barriers, and the prefactors are given in Tables II and III.

Constant-temperature MD results with the EPs can be used to compute the "dynamic barriers" for He diffusion, where the effect of thermal vibration is naturally taken into account. For this purpose, the jump frequencies between the various

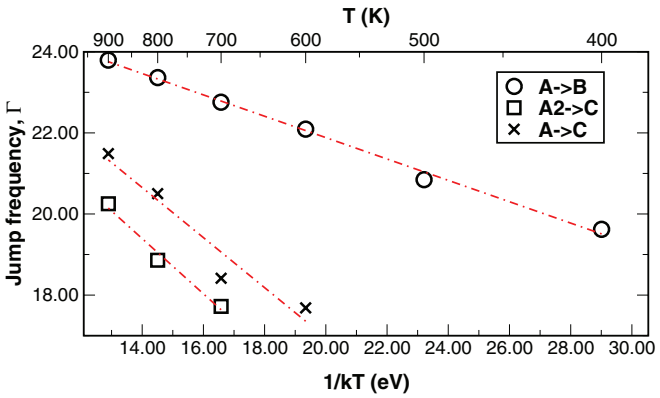

FIG. 14. (Color online) Arrhenius plot: logarithm of the jump frequency of an interstitial He for the $A \rightarrow B$, $A2 \rightarrow C$, and $A \rightarrow C$ hops in $\Sigma 5(310)$ GB versus temperature.

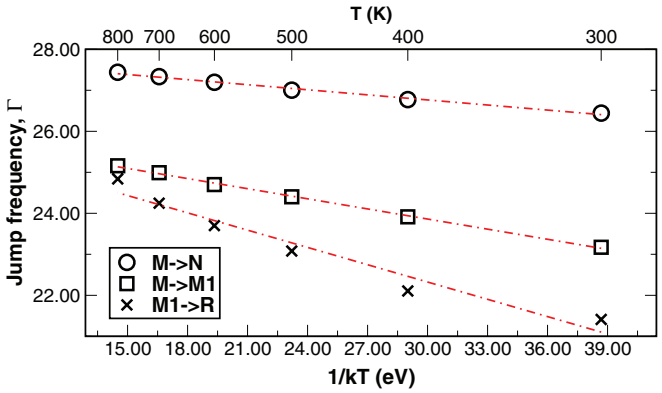

FIG. 15. (Color online) Arrhenius plot: logarithm of the jump frequency of an interstitial He for the $M \rightarrow N$, $M \rightarrow M1$, and $M1 \rightarrow R$ hops in $\Sigma 9(114)$ GB versus temperature.

neighboring local minima were calculated, based on the MD simulations that were carried out from 300 K to 900 K for both the $\Sigma 5(310)$ and the $\Sigma 9(114)$ GBs. Each simulation was 50 ns long and the counted jumping events range from 2 to 621 for the $\Sigma 5(310)$ GB and from 12 to 28 191 for the $\Sigma 9(114)$ GB. Consistent with the static barrier estimations, the He atom stays confined within the GB region even at the highest temperature and its diffusion is overall parallel to the GB planes. The migration energies between the local minima are obtained by fitting the jump frequencies as a function of the temperature according to the Arrhenius law (Figs. 14 and 15). From Fig. 14, there are neither y nor xy jumps observed in $\Sigma 5(310)$ GB at low temperatures (below 500 K). The finite-temperature results therefore confirm that the He atom diffusion is essentially 1D at low temperatures, as predicted by the static-barrier calculations. The obtained dynamic barriers for the 1D and the 2D paths are respectively 0.26 eV and 0.68 eV. On the other hand, both the close-neighbor and the long jumps are observed in the $\Sigma 9(114)$ GB for all the temperatures (Fig. 15), and the dynamic barriers range from 0.04 eV to 0.14 eV. The He atoms are confirmed to perform a 1D diffusion within a few layers around the GB plane. The obtained dynamic barriers are generally slightly lower than the static barriers (Tables II and III, except for the barrier of the $M1 \rightarrow R$ long jump (0.14 eV) in $\Sigma 9(114)$, which is much lower than the static barrier (0.53 eV).

IV. CONCLUSIONS

Density functional theory and empirical potentials are employed to investigate the lowest-energy sites and migration mechanisms of He in three α-Fe grain boundaries: $\Sigma 5(310)/[001]$, $\Sigma 9(114)/[110]$, and $\Sigma 3(111)/[110]$. Before the defect calculations, we have shown that structural relaxations, including simulated annealing and atom removal, are crucial for locating the stable GB structure at a given temperature regime. For instance, a negative vacancy formation energy is a signature of an unstable GB structure, so the offending atom should be removed.

After the structural optimizations, we have checked that the vacancy formation energies are all positive and smaller in the GBs than in the bulk. However, the preferential site for a vacancy is not systematically at the interface layer. A roughly linear relationship was found between the unrelaxed formation energies and the variation of magnetic moments of the neighboring Fe atoms, consistent with the magnetovolume effect.

Then, the He formation energies for all the substitutional and interstitial sites in the $\Sigma 5(310)$ and the $\Sigma 9(114)$ GBs were evaluated. As expected, the obtained values are much smaller near the GBs than in the bulk, indicating a strong He segregation tendency. In addition, we note that at variance with the bulk Fe case, the formation energy of an interstitial He is either lower than or similar to that of a substitutional He in both of the GBs. Also, interestingly, the He formation energies in the GBs are not dictated only by the atomic volume of the He atom. The vacancy formation energy and the energy cost due to the Fe-lattice distortion may play an important role.

Finally, both static and dynamic barriers for interstitial He diffusion in the GBs are calculated. We note that although the diffusion details and precise paths are GB dependent, some common features are found for the both $\Sigma 5(310)$ and $\Sigma 9(114)$ GBs: (1) All the barriers found for He diffusion along the GBs are much lower than the He-GB dissociation energy. Consistently, while diffusing, the He atom remains confined in the GB region up to 900 K. (2) Fast one-dimensional paths are found for both GBs, making the He diffusion highly anisotropic along the GBs. In general, we expect an anisotropic diffusion along GBs presenting ordered structures. (3) All the diffusion barriers obtained in the GBs are higher than the interstitial He diffusion barrier in the bulk. However, the latter conclusion does not necessarily imply that the He diffusion along GBs is slower than in a bcc bulk, since the interstitial He in the GB may diffuse faster than the dominant He species in the bulk, i.e., the substitutional He.

ACKNOWLEDGMENTS

This work was supported by the National Natural Science Foundation of China (NSFC) through Grant No. 51061130558 and by the ANR-NSFC joint project "HSunThEx" (2011-2013). All calculations were performed using resources from HPC-FF (in Judish, Germany) and from GENCI (Grants No. x2012096020 and No. x2013096020). C.C.F. acknowledges the support of the EFDA MAT-IREMEV program and fruitful discussions with S. Dudarev (CCFE, UK) and B. Legrand (CEA, France). Erin Hayward is acknowledged for a critical reading of the manuscript.

*chuchun.fu@cea.fr
†lgh@buaa.edu.cn

[1] H. Lefaix-Jeuland, S. Moll, T. Jourdan, and F. Legendre, J. Nucl. Mater. **434**, 152 (2013).
[2] P. L. Lane and P. J. Goodhew, Philos. Mag. A **48**, 965 (1983).
[3] B. Bokstein and I. Razumovskii, Interface Sci. **11**, 41 (2003).
[4] S. V. Divinski, H. Edelhoff, and S. Prokofjev, Phys. Rev. B **85**, 144104 (2012).

[5]R. Janisch and C. Elsasser, Phys. Rev. B **67**, 224101 (2003).
[6]R. Janisch and C. Elsasser, Int. J. Mater. Res. **100**, 1488 (2009).
[7]J. Shang, D. Zhao, and C. Wang, Acta Metall. Sin. **37**, 893 (2001).
[8]S. Gesari, M. Pronsato, and A. Juan, Surf. Rev. Lett. **9**, 1437 (2002).
[9]S.-Y. Wang, C.-Y. Wang, and D.-L. Zhao, J. Alloys Compd. **368**, 308 (2004).
[10]J.-X. Shang, X.-D. Zhao, F.-H. Wang, C.-Y. Wang, and H.-B. Xu, Comput. Mater. Sci. **38**, 217 (2006).
[11]E. Wachowicz, T. Ossowski, and A. Kiejna, Phys. Rev. B **81**, 094104 (2010).
[12]M. Yamaguchi, Y. Nishiyama, and H. Kaburaki, Phys. Rev. B **76**, 035418 (2007).
[13]Y. A. Du, L. Ismer, J. Rogal, T. Hickel, J. Neugebauer, and R. Drautz, Phys. Rev. B **84**, 144121 (2011).
[14]J. Rothaut, H. Schroeder, and H. Ullmaier, Philos. Mag. A **47**, 781 (1983).
[15]N. Gao, M. Victoria, J. Chen, and H. V. Swygenhoven, J. Phys.: Condens. Matter **23**, 245403 (2011).
[16]C.-C. Fu and F. Willaime, Phys. Rev. B **72**, 064117 (2005).
[17]B. Singh, T. Leffers, W. Green, and M. Victoria, J. Nucl. Mater. **125**, 287 (1984).
[18]K. Farrell, P. Maziasz, E. Lee, and L. Mansure, Radiat. Eff. **78**, 1 (1983).
[19]S. Zinkle and N. Ghoniem, Fusion Eng. Des. **51**, 55 (2000).
[20]H. Ullmaier, Nucl. Fusion **24**, 1039 (1984).
[21]A. Kimura, R. Kasada, R. Sugano, A. Hasegawa, and H. Matsui, J. Nucl. Mater. **283–287**, 827 (2000).
[22]F. Carsughi, H. Ullmaier, H. Trinkaus, W. Kesternich, and V. Zell, J. Nucl. Mater. **212–215**, 336 (1994).
[23]I. S. Batra, H. Ullmaier, and K. Sonnenberg, J. Nucl. Mater. **116**, 136 (1983).
[24]F. Gao, H. L. Heinisch, and R. J. Kurtz, J. Nucl. Mater. **367–370**, 446 (2007).
[25]F. Gao, H. L. Heinisch, and R. J. Kurtz, J. Nucl. Mater. **351**, 133 (2006).
[26]R. J. Kurtz and H. L. Heinisch, J. Nucl. Mater. **329–333**, 1199 (2004).
[27]L. Zhang, Y. Zhang, W. T. Geng, and G. H. Lu, Europhys. Lett. **98**, 17001 (2012).
[28]L. Zhang, X. L. Shu, S. Jin, Y. Zhang, and G. H. Lu, J. Phys.: Condens. Matter **22**, 375401 (2010).
[29]S. von Alfthan, P. D. Haynes, K. Kaski, and A. P. Sutton, Phys. Rev. Lett. **96**, 055505 (2006).
[30]J. Soler, E. Artacho, J. Gale, A. Garcia, J. Junquera, P. Ordejón, and D. Sanchez-Portal, J. Phys.: Condens. Matter **14**, 2745 (2002).
[31]C. C. Fu, F. Willaime, and P. Ordejón, Phys. Rev. Lett. **92**, 175503 (2004).
[32]G. J. Ackland, M. I. Mendelev, D. J. Srolovitz, S. Han, and A. V. Barashev, J. Phys.: Condens. Matter **16**, S2629 (2004).
[33]R. A. Aziz, A. R. Janzen, and M. R. Moldover, Phys. Rev. Lett. **74**, 1586 (1995).
[34]F. Gao, H. Deng, H. Heinisch, and R. Kurtz, J. Nucl. Mater. **418**, 115 (2011).
[35]C. H. Rycroft, G. S. Grest, J. W. Landry, and M. Z. Bazant, Phys. Rev. E **74**, 021306 (2006).
[36]G. Henkelman, B. P. Uberuaga, and H. Jónsson, J. Chem. Phys. **113**, 9901 (2000).
[37]G. Henkelman and H. Jónsson, J. Chem. Phys. **113**, 9978 (2000).
[38]C. C. Fu, J. Dalla Torre, F. Willaime, J.-L. Bocquet, and A. Barbu, Nat. Mater. **4**, 68 (2005).
[39]H. Amara, C. C. Fu, F. Soisson, and P. Maugis, Phys. Rev. B **81**, 174101 (2010).
[40]F. Soisson and C.-C. Fu, Phys. Rev. B **76**, 214102 (2007).
[41]E. Martinez and C.-C. Fu, Phys. Rev. B **84**, 014203 (2011).
[42]C.-C. Fu, M. Weissmann, and A. Saul, Surf. Sci. **481**, 97 (2001).
[43]G. H. Campbell, S. M. Foiles, P. Gumbsch, M. Rühle, and W. E. King, Phys. Rev. Lett. **70**, 449 (1993).
[44]G. Campbell, J. Belak, and J. Moriarty, Acta Mater. **47**, 3977 (1999).
[45]S. Suzuki, K. Abiko, and H. Kimura, Scr. Metall. **15**, 1139 (1981).
[46]S. von Alfthan, K. Kaski, and A. P. Sutton, Phys. Rev. B **76**, 245317 (2007).
[47]W. T. Geng, A. J. Freeman, and G. B. Olson, Phys. Rev. B **63**, 165415 (2001).
[48]J. X. Shang, D. Zhao, and C. Wang, Acta Metall. Sin. **37**, 893 (2001).
[49]W. Geng, A. Freeman, and G. Olson, Solid State Commun. **119**, 585 (2001).
[50]M. Yamaguchi, J. Jpn. Inst. Met. **72**, 657 (2008).
[51]M. Yamaguchi, M. Shiga, and H. Kaburaki, Mater. Trans. **47**, 2682 (2006).
[52]N. Gao, C.-C. Fu, M. Samaras, R. Schublin, M. Victoria, and W. Hoffelner, J. Nucl. Mater. **385**, 262 (2009).
[53]M. Shiga, J. Phys. Soc. Jpn. **50**, 2573 (1981).
[54]T. Yoshinori and N. Hiroki, J. Phys.: Condens. Matter **18**, 521 (2006).
[55]V. Heine, Phys. Rev. **153**, 673 (1967).
[56]M. J. Puska, R. M. Nieminen, and M. Manninen, Phys. Rev. B **24**, 3037 (1981).
[57]C. J. Ortiz, M. J. Caturla, C. C. Fu, and F. Willaime, Phys. Rev. B **75**, 100102(R) (2007).
[58]R. Vassen, H. Trinkaus, and P. Jung, Phys. Rev. B **44**, 4206 (1991).